

## Speed of electronic phase propagation in BaFe<sub>2</sub>As<sub>2</sub> revealed by dilatometry

Xin Qin<sup>1,2</sup>, Xingyu Wang,<sup>3</sup> Wenshan Hong,<sup>1</sup> Mengqiao Geng,<sup>1,2</sup> Yuan Li<sup>1</sup>, Huiqian Luo<sup>1,3</sup>, Shiliang Li,<sup>3</sup> and Yang Liu<sup>1,2,\*</sup>

<sup>1</sup>International Center for Quantum Materials, Peking University, Haidian, Beijing 100871, China

<sup>2</sup>Hefei National Laboratory, Hefei 230088, China

<sup>3</sup>Beijing National Laboratory for Condensed Matter Physics, Institute of Physics, Chinese Academy of Sciences, Beijing 100190, China



(Received 1 December 2023; revised 25 March 2024; accepted 26 March 2024; published 26 April 2024)

Thermal expansion offers deep insights into phase transitions in condensed-matter physics. Utilizing an advanced ac temperature dilatometer with picometer resolution, this study clearly resolves the antiferromagnetic and structural transition in BaFe<sub>2</sub>As<sub>2</sub>. The implementation of temperature oscillation reveals a hysteresis near the transition temperature,  $T_N$ , with unprecedented resolution. Unexpectedly, we find that the hysteretic width exhibits a universal dependence on the parameters of temperature oscillation and the sample's longitudinal dimension, which, in turn, reveals a finite transition speed. Our quantitative analysis shows that this phase boundary propagates at a mere 188  $\mu\text{m/s}$ —a speed 7 orders of magnitude slower than acoustic waves. It suggests a hidden thermodynamic constraint imposed by the electronic degrees of freedom. Our research not only sheds light on the dynamics of phase transitions between different correlated phases, but also establishes high-precision dilatometry as a powerful tool for material studies. This measurement technique, when properly modified, can be extended to studies of other material properties, such as piezoelectric, magnetostriction, and elastic modulus.

DOI: 10.1103/PhysRevApplied.21.L041003

*a. Introduction.* Phase transitions are of great interest in the study of materials, where a variety of degrees of freedom are often coupled together. It is important to experimentally differentiate closely related transitions, as well as to identify the primary driving force behind the transition. Because density is a true scalar that remains invariant under all symmetry operations relevant to solids, it is expected to have symmetry-allowed coupling to all phase transitions. As a result, accurately measured density can be used for detection and classification of phase transitions. In practice, this is often done with length measurements, such as the linear thermal-expansion coefficient,  $\alpha$  [1–6]. Along with atomic microscope piezocantilevers, strain gauges, piezobenders, and x-ray diffractometers [7–10], the most used and accurate dilatometer is based on plate capacitors. The length change of the sample,  $\Delta L$ , is captured through monitoring the capacitance between the sample's upper surface and a metal reference surface, and  $\alpha$  is deduced by numerical differentiation,  $\alpha = L^{-1}dL/dT$  [11–16]. Unfortunately, the sample is always at equilibrium, because this method needs an ultrahigh temperature uniformity of the whole mechanical structure to achieve its

high accuracy, and its capacitance measurement limits the temperature-varying speed to about  $10^{-3}$  K/s.

In condensed-matter physics, the dynamic behavior of transitions is always attractive and many techniques have been implemented [17–21]. Limited by either resolution or slow response, conventional dilatometers are not suitable for studying the dynamic procedure of phase transitions. Here, we present an alternative approach for measuring thermal expansion with picometer resolution using optical interferometers. Using oscillating temperature, we can analyze the dynamic response of thermal expansion in the frequency domain. As a demonstration, we examine the antiferromagnetic phase transitions in BaFe<sub>2</sub>As<sub>2</sub> [22–25]. Our systematic investigation reveals a hysteresis that originates from the nonequilibrium state of the sample near the transition temperature,  $T_N$ . The width of the hysteresis in temperature is proportional to the sample thickness,  $L$ ; the frequency; and the amplitude of the temperature oscillation,  $\delta T$ . Thanks to continuous perturbation by  $\delta T$ , this hysteresis is likely a manifestation of the fact that the phase transitions are not infinitely sharp in time and the phase boundary propagates with a finite speed. The measured speed, approximately equal to 188  $\mu\text{m/s}$ , is significantly lower than the acoustic velocity, thus shining light on the complex nature of domain-boundary dynamics.

\*Corresponding author: liuyang02@pku.edu.cn

*b. Experimental setup.* We use BaFe<sub>2</sub>As<sub>2</sub>, the parent compound of “122” Fe-based superconductors, an ideal prototypical example of phase transition(s) with coupled degrees of freedom, for demonstration. It is generally believed to have a two-step phase transition when the temperature is lowered [22–25], i.e., a second-order structural transition at  $T_S = 134.5$  K followed by a first-order magnetic transition at  $T_N = 133.75$  K [26,27]. An electronic nematic phase is reported between  $T_S$  and  $T_N$  [28–32]. We study four single-crystal as-grown samples (S1–S4), with typical in-plane sizes of  $(2\text{--}4)\times(2\text{--}4)$  mm<sup>2</sup> and different thicknesses  $L = 430, 210, 400$ , and  $75$   $\mu\text{m}$ , respectively. Samples S1 and S2 are cleaved from the same piece, while S3 and S4 come from another one.

The samples are placed on the upper surface of a sapphire sample holder with extremely thin ( $\sim 5$   $\mu\text{m}$ ) N-Grase for better thermal conductivity, so they are considered to be free-standing, and thermal expansion is measured along the *c*-axis direction. There are three pairs of evaporated Pt wires on the lower surface of the sample holder, which are used as a thermometer and ac and dc heaters, respectively; see Fig. 1(b). We measure the thermometer’s resistance and calibrate it by the cryostat temperature when the heaters are switched OFF. The real-time sample temperature can be separated into a slowly sweeping dc part,  $T_0$ , by the dc heater and an ac oscillation,  $\delta T$ , by the ac heater.  $\delta T$  of the sample induces an oscillation,  $\delta L$ , in sample thickness, and then the thermal-expansion coefficient,  $\alpha$ , can be deduced from  $\alpha = L^{-1}\delta L/\delta T$ , with the measurement of  $\delta L$  and  $\delta T$  by using the lock-in technique. We are able to achieve a comparable performance to that of the reported capacitive dilatometry [16], i.e., picometer resolution in  $\delta L$  amplitude,  $\langle \delta L \rangle$ , and millikelvin resolution in  $\delta T$  amplitude,  $\langle \delta T \rangle$ , with a dynamic measurement nature.

The  $\delta L$  measurement of our dilatometer is based on a high-resolution optical fiber Michelson interferometer, with the output interference light intensity,  $I$ , depending on the phase difference,  $\Phi$ , between the probing and reference light beams of  $I = I_0[1 + \cos(\Phi)]$ . We can tune the optical length of the two beams by applying the modulation and feedback voltages,  $V_M$  and  $V_F$ , respectively, to the corresponding piezoelectric transducer (PZT) rings; see Fig. 1(a).  $\Phi$  consists of three different components: the modulation phase,  $\phi_M = C \cos(2\pi f_M t) \propto V_M$ ; the ac phase signal,  $\phi_S = 4\pi/\lambda\delta L$ , where  $\delta L = \alpha L \delta T$  is the sample’s thermal expansion induced by ac temperature oscillation,  $\delta T$ ; and the slowly varying  $\phi_0$  caused by thermal drift.  $C$  and  $f_M$  are the amplitude and frequency of modulation, respectively;  $\alpha$  is the thermal-expansion coefficient; and  $\lambda = 1550$  nm is the optical wavelength. We compensate for thermal drift using the feedback voltage,  $V_F$ , so that  $\phi_0$  can be neglected. According to the Jacobi-Anger expansion, the amplitudes of the output optical power’s first- and second-harmonic components at  $f_M$  and  $2f_M$  are  $I_1 = I_0 J_1(C) \sin(\phi_S(t))$  and  $I_2 = I_0 J_2(C) \cos(\phi_S(t))$ ,

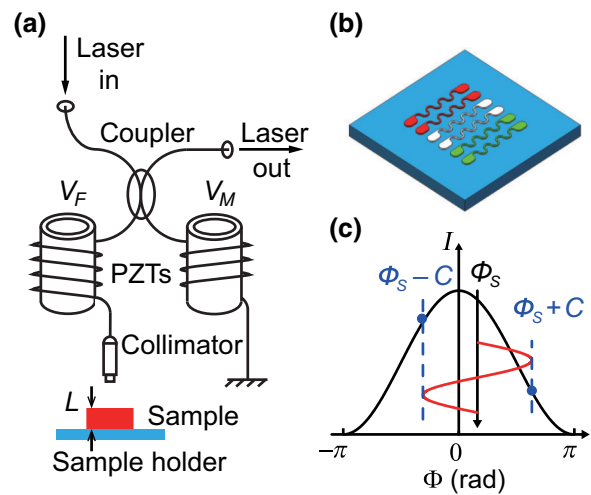


FIG. 1. (a) Our dilatometer uses a fiber Michelson interferometer. Probing (left) and reference (right) arms are wound around cylindrical PZT rings, through which we can tune their lengths using the modulation and feedback voltages,  $V_M$  and  $V_F$ , respectively.  $V_M$  generates a phase modulation,  $\phi_M = C \cos(\omega_M t)$ , and  $V_F$  eliminates the thermal drift,  $\Phi_0 \approx 0$ . (b) Detailed cartoon of the sapphire sample holder. White, red, and green Pt wires are used as the thermometer and ac and dc heaters, respectively. (c) Interference light intensity,  $I = \cos(\Phi)$ , is an odd function of the two beams’ phase difference,  $\Phi = \Phi_M + \phi_S$ , where  $\phi_S$  originates from thermal expansion induced by the ac temperature oscillation.  $\Phi$  oscillates between  $\phi_S \pm C$ , and the optical power difference between the two  $\Phi$  extremes has a positive dependence on  $\phi_S$ ; see text for a detailed description of our measurement principle.

respectively;  $J_N$  is the Bessel function of the  $N$ th order. We measure  $I_1$  and  $I_2$  using the lock-in technique to deduce the sample’s thermal expansion through

$$\delta L = \frac{\lambda}{4\pi} \tan^{-1} \left( \frac{J_2(C)I_1}{J_1(C)I_2} \right) \approx \frac{J_2(C)\lambda}{4\pi J_1(C)I_2} I_1.$$

The phase-modulation frequency,  $f_M$ , is typically a few kilohertz; the ac temperature oscillation frequency,  $f_S$ , is 100 and 250 mHz; the feedback eliminates drift at  $\lesssim 0.1$  Hz; and the  $T_0$  sweeping rate is  $10^{-4}$  K/s. Our resolution of  $\langle \delta L \rangle$  is as small as about 5 pm when using 50-mHz-resolution bandwidth, so that we can use  $\langle \delta T \rangle$  as small as 5 mK; see Fig. 3. More details about the design, principle, and performance of our dilatometer can be found in Ref. [33].

*c. Experimental results.* Figure 2(a) shows typically measured  $\delta T$  and  $\delta L$  oscillations ( $T_0 \simeq 130$  K). The phases of these two oscillations are perfectly aligned, leading to a linear line in Fig. 2(b), the slope of which is the thermal-expansion coefficient,  $\alpha$ .  $\alpha$  can be measured using the lock-in technique by separating  $\delta L$  oscillation into in-phase and out-of-phase components with reference to

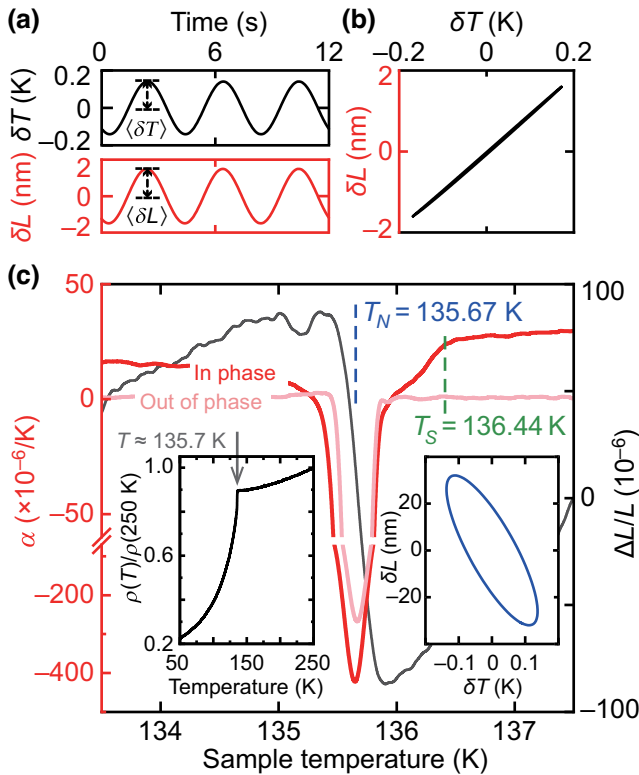


FIG. 2. (a) Typical  $\delta L$  and  $\delta T$  oscillations measured at  $T_0 \simeq 130 \text{ K}$ . (b)  $\delta L/L$  versus  $\delta T$  plot of data given in (a). (c) In-phase (red) and out-of-phase (pink) thermal-expansion coefficient,  $\alpha$ , by comparing  $\delta L$  and  $\delta T$  oscillations. dc thickness variation,  $\Delta L$  (black), is deduced from  $GV_F$ . Data measured from sample S1 using  $\delta T$  frequency  $f_S = 250 \text{ mHz}$  and amplitude  $\langle \delta T \rangle = 0.14 \text{ K}$ . Magnetic transition temperature,  $T_N$ , and structural transition temperature,  $T_S$ , are marked by blue and green dashed lines, respectively. Left inset is the zero-field normalized resistivity in  $a$ - $b$  plane, and the right inset illustrates the  $\delta L$  versus  $\delta T$  hysteresis loop at  $T = T_N$ .

$\delta T$ . The in-phase component of  $\alpha$  is finite and its out-of-phase component remains nearly zero at temperatures away from  $T_N$ , i.e.,  $T > 136.5 \text{ K}$  or  $T < 135 \text{ K}$ , suggesting that the sample is at equilibrium and has a uniform phase. Besides the ac differential measurement of  $\alpha$ , we can also measure the sample's dc thickness change directly from the feedback voltage,  $V_F$ , through  $\Delta L = GV_F$ , where  $G = |\lambda/\pi \times d\Phi/dV_F|$  is the feedback gain.

In Fig. 2(c),  $\Delta L$  taken from sample S1 ( $L \simeq 430 \mu\text{m}$ ) exhibits a jump of about  $\Delta L/L \simeq 1.5 \times 10^{-4}$  at  $T_N = 135.67 \text{ K}$ , where the in-phase component of  $\alpha$  has a huge negative peak. This first-order phase transition is consistent with our characterization of resistivity shown in the left inset of Fig. 2(c) and previous reports that the sample makes a transition from a high-temperature paramagnetic (PM) phase to a low-temperature antiferromagnetic (AFM) phase [26]. Unlike the smooth and gradual increase on the low-temperature side of  $T_N$ ,  $\alpha$  exhibits a clear kink

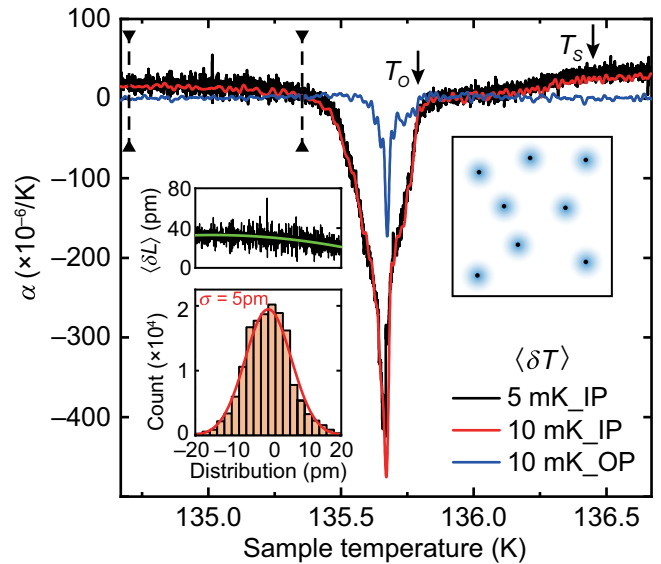


FIG. 3.  $\alpha$  measured using extremely small  $\langle \delta T \rangle = 5$  and  $10 \text{ mK}$  at  $250 \text{ mHz}$  from S2 (IP and OP are in-phase and out-of-phase parts of  $\alpha$ , respectively). Abrupt  $\alpha$  drop at  $T_O \simeq T_N + 0.1 \text{ K}$  suggests the formation of the AFM domains (blue dots) in the PM bath, as illustrated by the right-inset cartoon. Black dots represent the condensation nuclei of AFM domains, which might be defects. Left inset shows measured  $\langle \delta L \rangle$  in the range marked by the two vertical bars using  $50\text{-mHz}$ -resolution bandwidth. We deduce  $5\text{-pm}$  resolution from the histogram of  $\langle \delta L \rangle$  noise by subtracting the fitted green curve.

in Fig. 2(c) at  $T_S \simeq 136.44 \text{ K}$ , signaling the second-order phase transition. This is consistent with work by Kim *et al.* [26], who observed a structural transition from a tetragonal to an orthorhombic lattice by high-resolution x-ray diffraction studies.

The small  $\langle \delta T \rangle$  provides a high resolution in temperature and reveals many features near the phase transition. Figure 3 shows  $\alpha$  measured from sample S2 ( $L \simeq 210 \mu\text{m}$ ), where  $\langle \delta T \rangle$  is as small as 5 and  $10 \text{ mK}$ . The  $\alpha$  peak of the S2 data is narrow and deep, providing evidence of the sample's high quality, since most of its bulk has the same  $T_N$ . The temperature resolutions are about 10 and  $20 \text{ mK}$  and both of them are smaller than the detailed features of the  $\alpha$  peak. Clear kinks in  $\alpha$  appear at  $T_S$  about  $0.8 \text{ K}$  above  $T_N$ , similar to sample S1, providing evidence of a strong link between these two transitions. Additionally, we observe an extra abrupt change of  $\alpha$  at  $T_O \simeq T_N + 0.1 \text{ K}$ , which can be qualitatively explained by the formation of AFM clusters around condensation nuclei, such as defects, while a substantial part of the sample remains PM; see the inset of Fig. 3 [31].

Interestingly, the phases of  $\delta L$  and  $\delta T$  oscillation are no longer aligned near  $T_N$ , as signaled by the large out-of-phase component of  $\alpha$  in Figs. 2 and 3. In other words,  $\delta L$  versus  $\delta T$  exhibits a hysteretic ellipse, as shown in the right inset of Fig. 2(c). We choose data for sample S1 at

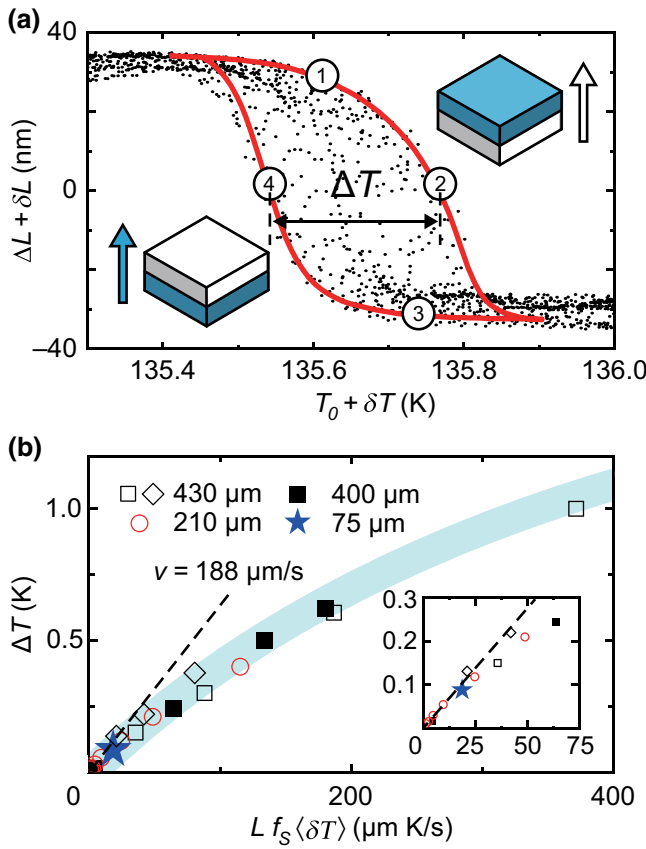


FIG. 4. (a) Thickness-temperature hysteresis. Data measured using  $f_S = 100\text{ mHz}$  and  $\langle \delta T \rangle = 0.25\text{ K}$ . Note that the peak-to-peak amplitude of temperature oscillation is  $2\langle \delta T \rangle = 0.5\text{ K}$ . We highlight one thermal cycle with a thick-red line and mark four positions in the loop. Inset cartoons illustrate the coexistence of PM (white) and AFM (blue) phases and the propagation of their phase boundary. (b) Summary of  $\Delta T$  versus  $L f_S \langle \delta T \rangle$  measured from different samples. We use  $f_S = 100$  (open diamond) and  $250\text{ mHz}$  (open square) for sample S1 data, and  $f_S = 250\text{ mHz}$  for all other data. Uncertainty is comparable to the symbol size. Inset is a magnified plot near zero.

$f_S = 100\text{ mHz}$  and  $\langle \delta T \rangle \simeq 0.25\text{ K}$  as an example and sum dc component  $\Delta L$ , induced by sweeping of the dc temperature  $T_0$  and measured by  $V_F$ , and ac component  $\delta L$ , induced by the ac temperature change  $\delta T$  and measured by the lock-in technique, as the real-time thickness of sample  $\Delta L + \delta L$  and plot it as a function of the real-time temperature  $T_0 + \delta T$  [black dots in Fig. 4(a)]. We highlight the relationship between  $\Delta L + \delta L$  and  $T_0 + \delta T$  within one period of  $\delta T$  at  $T_0 = T_N$  with a red line, and all the real-time-thickness dots in the phase-transition region fall inside the area enclosed by this red line. The clear square hysteresis loop indicates that the sample is off equilibrium and has two coexisting phases at the transition.

A detailed and accurate description of this hysteresis involves the dynamic process of the phase transition, which is rather complicated and beyond the scope of this

article. Fortunately, we can understand the observed phenomenon using a simple model. In Fig. 4(a), we highlight one thermal loop with a red line, and the four numbers mark four different conditions. The sample starts from a uniform AFM phase at low temperature. When the temperature increases through  $T_N$  at spot 1, the PM phase appears at the sample's bottom surface, which is thermally anchored to the sample holder. The PM domain grows and the phase boundary propagates upward until it reaches the sample's top surface. When we cool the sample back through  $T_N$  at spot 3, the AFM phase forms at the bottom of the sample and grows upward. We can identify two specific positions, labeled 2 and 4 in Fig. 4(a), which correspond to the midpoint of the phase transition. At these two points, the sample is divided in half into AFM and PM phases; see the inset cartoons. We define the distance between the two points,  $\Delta T \simeq 0.22\text{ K}$ , as the width of the hysteresis loop.

It is worthwhile mentioning several facts about  $\Delta T$ . First, the hysteresis width is not limited by the range of temperature oscillation, i.e., the peak-to-peak amplitude,  $2\langle \delta T \rangle$ . For example,  $\Delta T \simeq 0.22\text{ K}$  in Fig. 4(a) is about 40% of  $2\langle \delta T \rangle \simeq 0.5\text{ K}$ . This ratio becomes even smaller with lower frequency or a thinner sample. Second, in contrast with systems such as supercooled pristine water, which has a liquid configuration well below its crystallization temperature if cooled slowly [34], the finite-width hysteresis loop only occurs because the temperature is changing “too fast” for this phase transition.  $\Delta T$  vanishes when the amplitude or frequency of  $\delta T$  approaches zero. The ratio of the out-of-phase part to the in-phase part of  $\alpha$  can symbolize  $\Delta T$  qualitatively. So, the extremely narrow peak of the out-of-phase part of  $\alpha$  at  $\langle \delta T \rangle = 10\text{ mK}$  shown in Fig. 3, compared with the width peak at  $\langle \delta T \rangle = 0.14\text{ K}$  shown in Fig. 2(c), also indicates that the transition becomes infinitely sharp if we sweep the ac temperature change sufficiently slowly, which is consistent with previous capacitive dilatometry studies in which no hysteresis is seen.

We measure the hysteresis loop from different samples using different  $\delta T$  frequencies,  $f_S$ , and amplitudes,  $\langle \delta T \rangle$ . We use  $f_S = 100$  and  $250\text{ mHz}$  to measure S1, and  $f_S = 250\text{ mHz}$  for the other samples. We find that  $\Delta T$  is proportional to the sample thickness,  $L$ ; the ac temperature oscillation frequency,  $f_S$ ; and the amplitude,  $\langle \delta T \rangle$ . We summarize  $\Delta T$  as a function of  $L f_S \langle \delta T \rangle$  in Fig. 4(b). It is quite remarkable that all data points collapse onto the same curve highlighted by the blue band. We note that the phase boundary propagates by a distance  $L/2$  to the midpoint of the sample from its bottom surface at spots 2 and 4, as shown in the cartoons of Fig. 4(a), and  $f_S \langle \delta T \rangle$  is the maximum temperature-change rate. Therefore, the slope of the blue curve corresponds to the propagation speed of the phase boundary, which is  $v = 188\text{ }\mu\text{m/s}$  at small  $L f_S \langle \delta T \rangle$ . This speed is 7 orders of magnitude slower than that of acoustic waves [35]. The constraint on the phase-boundary

propagation speed is likely related to the magnetoelastic nature of the transition at  $T_N$ , where the electronic degrees of freedom correlate with lattice deformation. The formation of structural domains [36] is not directly related to the hysteresis, since the domains span the whole sample along the  $c$ -axis direction. However, it may be one of the reasons limiting the propagation speed by causing strain and dissipating energy.

*d. Conclusion.* Our study of the thermal-expansion coefficient of BaFe<sub>2</sub>As<sub>2</sub> using an interferometer-based dilatometer reveals interesting information about its magnetic transition. Our results clearly resolve the two-step transition, where the second-order structural transition appears at  $T_S$  and the first-order magnetic transition at  $T_N$ . Thanks to the extremely high resolution and “true” differential nature of our technique, we discover the samples’ thickness-temperature hysteresis loop at  $T_N$ . We can describe this dynamic process with a simple model, and our systematic study reveals the propagation speed of the phase boundary to be  $v = 188 \mu\text{m/s}$ . More research is needed to further understand the intrinsic origin of the phase-boundary propagation speed. This work highlights that ac temperature dilatometry with extraordinarily high resolution is a powerful probe of correlation effects in quantum materials, and it is a high-resolution approach for phase-transition research.

*Acknowledgments.* The work at PKU was supported by the National Key Research and Development Program of China (Grants No. 2021YFA1401900 and No. 2019YFA0308403), the Innovation Program for Quantum Science and Technology (Grant No. 2021ZD0302602), and the National Natural Science Foundation of China (Grants No. 92065104 and No. 12074010). The work at IOP was supported by the National Key Research and Development Program of China (Grants No. 2022YFA1403400 and No. 2021YFA1400400), and the Strategic Priority Research Program(B) of the Chinese Academy of Sciences (Grants No. XDB33000000 and No. GJTD-2020-01). We thank Mingquan He for valuable discussions.

- 
- [1] F. Hardy, N. J. Hillier, C. Meingast, D. Colson, Y. Li, N. Barišić, G. Yu, X. Zhao, M. Greven, and J. S. Schilling, Enhancement of the critical temperature of HgBa<sub>2</sub>CuO<sub>4+δ</sub> by applying uniaxial and hydrostatic pressure: Implications for a universal trend in cuprate superconductors, *Phys. Rev. Lett.* **105**, 167002 (2010).
  - [2] M. He, X. Wang, L. Wang, F. Hardy, T. Wolf, P. Adelmann, T. Bruckel, Y. Su, and C. Meingast, Uniaxial and hydrostatic pressure effects in alpha-RuCl<sub>3</sub> single crystals via thermal-expansion measurements, *J. Phys.-Condens. Matter* **30**, 385702 (2018).

- [3] R. Küchler, P. Gegenwart, J. Custers, O. Stockert, N. Caroca-Canales, C. Geibel, J. G. Sereni, and F. Steglich, Quantum criticality in the cubic heavy-fermion system CeIn<sub>3-x</sub>Sn<sub>x</sub>, *Phys. Rev. Lett.* **96**, 256403 (2006).
- [4] S. Zaum, K. Grube, R. Schäfer, E. D. Bauer, J. D. Thompson, and H. V. Löhneysen, Towards the identification of a quantum critical line in the ( $p$ ,  $B$ ) phase diagram of CeCoIn<sub>5</sub> with thermal-expansion measurements, *Phys. Rev. Lett.* **106**, 087003 (2011).
- [5] R. Küchler, N. Oeschler, P. Gegenwart, T. Cichorek, K. Neumaier, O. Tegus, C. Geibel, J. A. Mydosh, F. Steglich, L. Zhu, and Q. Si, Divergence of the Grüneisen ratio at quantum critical points in heavy fermion metals, *Phys. Rev. Lett.* **91**, 066405 (2003).
- [6] C. Meingast, F. Hardy, R. Heid, P. Adelmann, A. Böhrer, P. Burger, D. Ernst, R. Fromknecht, P. Schweiss, and T. Wolf, Thermal expansion and Grüneisen parameters of Ba(Fe<sub>1-x</sub>Co<sub>x</sub>)<sub>2</sub>As<sub>2</sub>: A thermodynamic quest for quantum criticality, *Phys. Rev. Lett.* **108**, 177004 (2012).
- [7] R. Grössinger and H. Müller, New device for determining small changes in length, *Rev. Sci. Instrum.* **52**, 1528 (1981).
- [8] G. O. J. B. F. Figgins and D. P. Riley, The thermal expansion of aluminium at low temperatures as measured by an x-ray diffraction method, *Philos. Mag.: A J. Theor. Exp. Appl. Phys.* **1**, 747 (1956).
- [9] Y. Gu, B. Liu, W. Hong, Z. Liu, W. Zhang, X. Ma, and S. Li, A temperature-modulated dilatometer by using a piezobender-based device, *Rev. Sci. Instrum.* **91**, 123901 (2020).
- [10] L. Wang, G. M. Schmiedeshoff, D. E. Graf, J.-H. Park, T. P. Murphy, S. W. Tozer, E. Palm, J. L. Sarrao, and J. C. Cooley, Application of an atomic force microscope piezocantilever for dilatometry under extreme conditions, *Meas. Sci. Technol.* **28**, 065006 (2017).
- [11] M. Rotter, H. Müller, E. Gratz, M. Doerr, and M. Loewenhaupt, A miniature capacitance dilatometer for thermal expansion and magnetostriction, *Rev. Sci. Instrum.* **69**, 2742 (1998).
- [12] R. S. Manna, B. Wolf, M. de Souza, and M. Lang, High-resolution thermal expansion measurements under helium-gas pressure, *Rev. Sci. Instrum.* **83**, 085111 (2012).
- [13] R. Küchler, T. Bauer, M. Brando, and F. Steglich, A compact and miniaturized high resolution capacitance dilatometer for measuring thermal expansion and magnetostriction, *Rev. Sci. Instrum.* **83**, 095102 (2012).
- [14] S. Abe, F. Sasaki, T. Oonishi, D. Inoue, J. Yoshida, D. Takahashi, H. Tsujii, H. Suzuki, and K. Matsumoto, A compact capacitive dilatometer for thermal expansion and magnetostriction measurements at millikelvin temperatures, *Cryogenics* **52**, 452 (2012).
- [15] R. Küchler, A. Wörl, P. Gegenwart, M. Berben, B. Bryant, and S. Wiedmann, The world’s smallest capacitive dilatometer, for high-resolution thermal expansion and magnetostriction in high magnetic fields, *Rev. Sci. Instrum.* **88**, 083903 (2017).
- [16] R. Küchler, R. Wawrzyniczak, H. Dawczak-Debicki, J. Gooth, and S. Galeski, New applications for the world’s smallest high-precision capacitance dilatometer and its stress-implementing counterpart, *Rev. Sci. Instrum.* **94**, 045108 (2023).

- [17] S. O. Mariager, F. Pressacco, G. Ingold, A. Caviezel, E. Möhr-Vorobeva, P. Beaud, S. L. Johnson, C. J. Milne, E. Mancini, S. Moyerman, E. E. Fullerton, R. Feidenhans'l, C. H. Back, and C. Quitmann, Structural and magnetic dynamics of a laser induced phase transition in FeRh, *Phys. Rev. Lett.* **108**, 087201 (2012).
- [18] S. L. Johnson, *et al.*, Femtosecond dynamics of the collinear-to-spiral antiferromagnetic phase transition in CuO, *Phys. Rev. Lett.* **108**, 037203 (2012).
- [19] I. Radu, K. Vahaplar, C. Stamm, T. Kachel, N. Pontius, H. A. Dürr, T. A. Ostler, J. Barker, R. F. L. Evans, R. W. Chantrell, A. Tsukamoto, A. Itoh, A. Kirilyuk, T. Rasing, and A. V. Kimel, Transient ferromagnetic-like state mediating ultrafast reversal of antiferromagnetically coupled spins, *Nature* **472**, 205 (2011).
- [20] K. A. Seu, S. Roy, J. J. Turner, S. Park, C. M. Falco, and S. D. Kevan, Cone phase and magnetization fluctuations in Au/Co/Au thin films near the spin-reorientation transition, *Phys. Rev. B* **82**, 012404 (2010).
- [21] S. Yoshimoto, Y. Tabata, T. Waki, and H. Nakamura, Novel slow dynamics of phase transition in the partially ordered frustrated magnet DyRu<sub>2</sub>Si<sub>2</sub>, *J. Phys. Soc. Jpn.* **92**, 094705 (2023).
- [22] Q. Huang, Y. Qiu, W. Bao, M. A. Green, J. W. Lynn, Y. C. Gasparovic, T. Wu, G. Wu, and X. H. Chen, Neutron-diffraction measurements of magnetic order and a structural transition in the parent BaFe<sub>2</sub>As<sub>2</sub> compound of FeAs-based high-temperature superconductors, *Phys. Rev. Lett.* **101**, 257003 (2008).
- [23] C. R. Rotundu, B. Freelon, T. R. Forrest, S. D. Wilson, P. N. Valdivia, G. Pinellas, A. Kim, J.-W. Kim, Z. Islam, E. Bourret-Courchesne, N. E. Phillips, and R. J. Birgeneau, Heat capacity study of BaFe<sub>2</sub>As<sub>2</sub>: Effects of annealing, *Phys. Rev. B* **82**, 144525 (2010).
- [24] S. D. Wilson, C. R. Rotundu, Z. Yamani, P. N. Valdivia, B. Freelon, E. Bourret-Courchesne, and R. J. Birgeneau, Universal magnetic and structural behaviors in the iron arsenides, *Phys. Rev. B* **81**, 014501 (2010).
- [25] S. D. Wilson, Z. Yamani, C. R. Rotundu, B. Freelon, E. Bourret-Courchesne, and R. J. Birgeneau, Neutron diffraction study of the magnetic and structural phase transitions in BaFe<sub>2</sub>As<sub>2</sub>, *Phys. Rev. B* **79**, 184519 (2009).
- [26] M. G. Kim, R. M. Fernandes, A. Kreyssig, J. W. Kim, A. Thaler, S. L. Bud'ko, P. C. Canfield, R. J. McQueeney, J. Schmalian, and A. I. Goldman, Character of the structural and magnetic phase transitions in the parent and electron-doped BaFe<sub>2</sub>As<sub>2</sub> compounds, *Phys. Rev. B* **83**, 134522 (2011).
- [27] T. R. Forrest, P. N. Valdivia, C. R. Rotundu, E. Bourret-Courchesne, and R. J. Birgeneau, The effects of post-growth annealing on the structural and magnetic properties of BaFe<sub>2</sub>As<sub>2</sub>, *J. Phys.: Condens. Matter* **28**, 115702 (2016).
- [28] A. E. Böhmer, Electronic nematic susceptibility of iron-based superconductors, *Comptes Rendus. Physique (En Ligne)* **17**, 90 (2016).
- [29] R. M. Fernandes, A. V. Chubukov, and J. Schmalian, What drives nematic order in iron-based superconductors?, *Nat. Phys.* **10**, 97 (2014).
- [30] E. Gati, L. Xiang, S. L. Bud'Ko, and P. C. Canfield, Role of the Fermi surface for the pressure-tuned nematic transition in the BaFe<sub>2</sub>As<sub>2</sub> family, *Phys. Rev. B* **100**, 064512 (2019).
- [31] X. Ren, L. Duan, Y. Hu, J. Li, R. Zhang, H. Luo, P. Dai, and Y. Li, Nematic crossover in BaFe<sub>2</sub>As<sub>2</sub> under uniaxial stress, *Phys. Rev. Lett.* **115**, 197002 (2015).
- [32] D. W. Tam, W. Wang, L. Zhang, Y. Song, R. Zhang, S. V. Carr, H. C. Walker, T. G. Perring, D. T. Adroja, and P. Dai, Weaker nematic phase connected to the first order antiferromagnetic phase transition in SrFe<sub>2</sub>As<sub>2</sub> compared to BaFe<sub>2</sub>As<sub>2</sub>, *Phys. Rev. B* **99**, 134519 (2019).
- [33] X. Qin, G. Cao, S. Liu, and Y. Liu, A high resolution dilatometer using optical fiber interferometer, *ArXiv:2311.16641*.
- [34] P. Gallo, K. Amann-Winkel, C. A. Angell, M. A. Anisimov, F. Caupin, C. Chakravarty, E. Lascaris, T. Loerting, A. Z. Panagiotopoulos, J. Russo, J. A. Sellberg, H. E. Stanley, H. Tanaka, C. Vega, L. Xu, and L. G. M. Pettersson, Water: A tale of two liquids, *Chem. Rev.* **116**, 7463 (2016).
- [35] Y. Xu, N. G. Petrik, R. S. Smith, B. D. Kay, and G. A. Kimmel, Growth rate of crystalline ice and the diffusivity of supercooled water from 126 to 262 K, *Proc. Natl. Acad. Sci.* **113**, 14921 (2016).
- [36] M. A. Tanatar, A. Kreyssig, S. Nandi, N. Ni, S. L. Bud'ko, P. C. Canfield, A. I. Goldman, and R. Prozorov, Direct imaging of the structural domains in the iron pnictides *A*Fe<sub>2</sub>As<sub>2</sub> (*A*=Ca, Sr, Ba), *Phys. Rev. B* **79**, 180508 (2009).